Colossal Ionic Conductivity at Interfaces of Epitaxial ZrO_2:Y_2O_3 /$SrTiO_3$ Heterostructures

J. García-Barriocanal *et al.*

Science **321**, 676 (2008);
DOI: 10.1126/science.1156393

Science (print ISSN 0036-8075; online ISSN 1095-9203) is published weekly, except the last week in December, by the American Association for the Advancement of Science, 1200 New York Avenue NW, Washington, DC 20005.

185 cm^{-1}, and its presence in the molecular beam could also explain the pronounced intensity of the central peak in the experimental spectrum. Ion mobility measurements, however, excluded the presence of major amounts of additional isomers for cationic and anionic Au_7. For experimental modes that were not present in the calculated spectrum of hexagonal Iso2—for example, at 165 cm^{-1} and 201 cm^{-1}—the mass-spectrometric intensity of Au_7Kr went down to below 30% of its original value when irradiated by FELIX, which set the upper limit for the abundance of other isomers. Therefore, although a minor contribution of Iso2 could not be ruled out, the capped triangle could be assigned as the dominant structural isomer of neutral Au_7 present in our experiment.

On comparison with the experimentally determined structures of the corresponding ionic species, we found that Au_7 is a cluster size, which changes its geometries for each charge state. Although the cation is highly symmetric and corresponds to the D_{6h} structure Iso2 (*12*), the anion forms a threefold edge-capped square (*11*). We found this structure to be a saddle point in our calculations for neutral Au_7 that relaxes into Iso1. The geometrical change as a function of cluster charge corresponds to a lessening of the average coordination as the electron density increases. Although the gold atoms in the cation have on average 3.43 nearest neighbors, this value decreases to 3.14 and 2.85 for the neutral and the anion, respectively. With additional electrons, the clusters favor more open structures.

Having shown that the experimental spectrum, in combination with theory, can be used to identify the geometry of the Au_7 cluster, we moved on to bigger sizes. Photoelectron spectroscopy and quantum-mechanical calculations have shown that anionic Au_{20}^- is a pyramid and has T_d symmetry (*14*). This structure has also been suggested to be the global minimum for neutral Au_{20} (*14*). The FIR-MPD spectrum we measured of the $Au_{20}Kr$ complex (Fig. 2A) was very simple, with a dominant absorption at 148 cm^{-1}, which already pointed to a highly symmetric structure. The calculated spectrum of tetrahedral Au_{20} was in agreement with the experiment (Fig. 2C, and see fig. S4 for the IR spectra of less stable isomers). In the FIR-MPD spectrum of $Au_{20}Kr_2$, weaker features occurred at low frequencies and were well reproduced by theory when the Kr ligands are included in the calculations (fig. S1). The strong absorption at 148 cm^{-1} corresponds to a triply degenerate vibration (t_2) in bare Au_{20} with T_d symmetry.

Theory predicts a truncated trigonal pyramid to be the minimum energy structure for neutral Au_{19} (*27*), for which the removal of a corner atom of the Au_{20} tetrahedron reduces the symmetry from T_d to C_{3v}. As a direct consequence, the degeneracy of the t_2 vibration of Au_{20} is lifted, and this mode splits into a doubly degenerate vibration (e) and a nondegenerate vibration (a_1) in Au_{19}. This splitting was observed in the vibrational spectrum of neutral Au_{19} (Fig. 2). The e vibration lies at 149 cm^{-1} and is hardly shifted as compared with the t_2 mode of Au_{20}. The a_1 vibration is blue-shifted by 18 cm^{-1} relative to the t_2 vibration in Au_{20}. The truncated pyramidal structure of Au_{19} can thus be inferred directly from the IR spectrum. We also found the C_{3v} structure of Au_{19} to be a minimum in our calculations, and the calculated vibrational spectrum fits the experimental one in terms of peak positions and relative intensities (Fig. 2D, and see fig. S5 for IR spectra of less-stable isomers). Again, the modifications in peak intensities induced by the Kr ligands agree well between theory and experiment (fig. S2).

We have shown that detailed structural information on small neutral gold nanoparticles can be obtained by means of vibrational spectroscopy. FIR-MPD is the only size-selective experimental technique available to date that allows for the structure determination of neutral metal clusters in the gas phase. It can be used to study the transition of 2D structures to 3D structures for neutral gold clusters as well as to study, for instance, ligand-induced geometrical modifications that are highly relevant in catalysis. With improved sensitivity for heavier masses, it will be possible to extend these measurements to larger clusters. Although spectral congestion may prohibit detailed analysis of nonsymmetric structures, we can expect symmetric and near-symmetric structures to remain identifiable, as they do for Au_{20} and Au_{19}. For instance, it should be possible to answer questions such as, is neutral Au_{55} icosahedral, or does it have a low-symmetry structure such as has been indicated for the anion (*28*)?

References and Notes

1. M. Haruta, N. Yamada, T. Kobayashi, S. Iijima, *J. Catal.* **115**, 301 (1989).
2. B. Hammer, J. K. Nørskov, *Nature* **376**, 238 (1995).
3. M. Valden, X. Lai, D. W. Goodman, *Science* **281**, 1647 (1998).
4. B. Yoon *et al.*, *Science* **307**, 403 (2005).
5. C. T. Campbell, *Science* **306**, 234 (2004).
6. P. P. Edwards, J. M. Thomas, *Angew. Chem. Int. Ed.* **46**, 5480 (2007).
7. C. Lemire, R. Meyer, S. Shaikhutdinov, H.-J. Freund, *Angew. Chem. Int. Ed.* **43**, 118 (2004).
8. G. Mills, M. S. Gordon, H. Metiu, *J. Chem. Phys.* **118**, 4198 (2003).
9. M. S. Chen, D. W. Goodman, *Science* **306**, 252 (2004).
10. Z. Y. Li *et al.*, *Nature* **451**, 46 (2008).
11. F. Furche *et al.*, *J. Chem. Phys.* **117**, 6982 (2002).
12. S. Gilb *et al.*, *J. Chem. Phys.* **116**, 4094 (2002).
13. S. Bulusu, X. Li, L.-S. Wang, X. C. Zeng, *Proc. Natl. Acad. Sci. U.S.A.* **103**, 8326 (2006).
14. J. Li, X. Li, H.-J. Zhai, L.-S. Wang, *Science* **299**, 864 (2003).
15. A. Lechtken *et al.*, *Angew. Chem. Int. Ed.* **46**, 2944 (2007).
16. X. Xing, B. Yoon, U. Landman, J. H. Parks, *Phys. Rev. B* **74**, 165423 (2006).
17. A. Fielicke *et al.*, *Phys. Rev. Lett.* **93**, 023401 (2004).
18. A. Fielicke, C. Ratsch, G. von Helden, G. Meijer, *J. Chem. Phys.* **122**, 091105 (2005).
19. A. Fielicke, G. von Helden, G. Meijer, *Eur. Phys. J. D* **34**, 83 (2005).
20. D. Oepts, A. F. G. van der Meer, P. W. van Amersfoort, *Infrared Phys. Technol.* **36**, 297 (1995).
21. Materials and methods are available as supporting material on *Science* Online.
22. The IR frequencies, calculated by DFT with TURBOMOLE V5.10 (*29*), were uniformly scaled by multiplication with a factor of 1.15.
23. V. Bonačić-Koutecký et al, *J. Chem. Phys.* **117**, 3120 (2002).
24. H. Häkkinen, U. Landman, *Phys. Rev. B* **62**, R2287 (2000).
25. J. Wang, G. Wang, J. Zhao, *Phys. Rev. B* **66**, 035418 (2002).
26. The influence of the rare-gas ligand on the IR absorption intensities is very similar to what has been found in photodissociation studies of cationic gold clusters in the visible region (*30*).
27. S. Bulusu, X. C. Zeng, *J. Chem. Phys.* **125**, 154303 (2006).
28. W. Huang *et al.*, *ACS Nano* **2**, 897 (2008).
29. R. Ahlrichs, M. Bär, M. Häser, H. Horn, C. Kölmel, *Chem. Phys. Lett.* **162**, 165 (1989).
30. A. N. Gloess, H. Schneider, J. M. Weber, M. M. Kappes, *J. Chem. Phys.* **128**, 114312 (2008).

31. The authors acknowledge support from the Cluster of Excellence Unifying Concepts in Catalysis coordinated by the Technische Universität Berlin and funded by the Deutsche Forschungsgemeinschaft. This work is supported by FOM by providing beam time for FELIX. We thank the FELIX staff for their skillful assistance, in particular J. Pluijgers and R. van Buuren, as well as K. Rademann for providing the cluster source. P.G. thanks the International Max Planck Research School Complex Surfaces in Material Science, and J.T.L. thanks the Alexander von Humboldt Foundation for funding.

Supporting Online Material

www.sciencemag.org/cgi/content/full/321/5889/674/DC1
Materials and Methods
Figs. S1 to S5

30 May 2008; accepted 23 June 2008
10.1126/science.1161166

Colossal Ionic Conductivity at Interfaces of Epitaxial ZrO_2:Y_2O_3/$SrTiO_3$ Heterostructures

J. Garcia-Barriocanal,[1] A. Rivera-Calzada,[1] M. Varela,[2] Z. Sefrioui,[1] E. Iborra,[3] C. Leon,[1] S. J. Pennycook,[2] J. Santamaria[1]*

The search for electrolyte materials with high oxygen conductivities is a key step toward reducing the operation temperature of fuel cells, which is currently above 700°C. We report a high lateral ionic conductivity, showing up to eight orders of magnitude enhancement near room temperature, in yttria-stabilized zirconia (YSZ)/strontium titanate epitaxial heterostructures. The enhancement of the conductivity is observed, along with a YSZ layer thickness–independent conductance, showing that it is an interface process. We propose that the atomic reconstruction at the interface between highly dissimilar structures (such as fluorite and perovskite) provides both a large number of carriers and a high-mobility plane, yielding colossal values of the ionic conductivity.

Solid oxide fuel cells (SOFCs) have emerged as a promising nonpolluting technology for the short-to-medium–term substitution of fossil fuels (*1*–*4*). The conversion efficiency of chemical into electrical energy is limited by the transport of oxygen anions through an elec-

trolyte material. So far, yttria-stabilized zirconia $(Y_2O_3)_x(ZrO_2)_{1-x}$ (YSZ) is the material mostly used in SOFCs because of its mechanical stability, chemical compatibility with electrodes, and high oxygen ionic conductivity. It is well known that doping ZrO_2 with Y_2O_3 stabilizes the cubic fluorite structure of ZrO_2 at room temperature and supplies the oxygen vacancies responsible for the ionic conduction, resulting in high values of the oxygen conductivity at high temperatures (*5*–*7*). A maximum value of 0.1 S/cm (where 1 S = 1 A/V) at 1000°C is observed for the 8 to 9 mole percent (mol %) yttria content (*2*–*4*). A severe drawback toward the final implementation of SOFCs is the relatively low room temperature ionic conductivity of this material, which imposes rather high operational temperatures around 800°C (*1*–*4*). The search for alternative electrolytes has not yet been successful in reaching the conductivity value of 0.01 S/cm desired for room temperature operation (*1*–*4*).

Only modest reductions in the operation temperature of SOFCs (500° to 700°C) can be anticipated with the recently proposed optimized electrolytes such as gadolinia-doped ceria and lanthanum gallates (*8*–*11*). On the other hand, the one to two orders of magnitude increase of the electrical conductivity reported (*12*–*14*) in nanocrystalline samples as compared with single crystals outlines the importance of processing as an alternative route to increasing conductivity values toward the desired levels. Because modern thin film growth techniques allow a precise control of layer thickness and morphology, they provide a pathway for the production of solid electrolytes with optimized properties. Maier *et al.* found a substantial increase of the dc ionic conductivity of superlattices of CaF_2 and BaF_2 when the thickness of the individual layers was decreased down to 16 nm, assigned to a size effect due to the space charge regions being smaller than the layer thickness (*15*, *16*). Kosacki *et al.* have reported enhanced conductivity in highly textured thin films of YSZ with thicknesses between 60 and 15 nm, reaching 0.6 S/cm at 800°C (*17*). Because reducing film thickness (and therefore increasing the fraction of material near the interface) produces such a noticeable conductivity enhancement, the interfaces themselves would seem to play a determining role in the outstanding conductivity properties observed.

To search for interface effects, we fabricated heterostructures where YSZ layers (with 8 mol % nominal yttria content) in the thickness range from 62 nm down to 1 nm were sandwiched between two 10-nm-thick layers of insulating $SrTiO_3$ (STO). Also, superlattices were grown, alternating 10-nm-thick STO films with YSZ layers with thickness between 62 and 1 nm (*18*). Figure 1A displays a low-magnification (inset) and a high-resolution annular dark field (or Z-contrast) image of a $[YSZ_{1nm}/STO_{10nm}]_9$ superlattice (with nine repeats), showing the excellent crystalline quality of the sample. The layers appear continuous and flat over long lateral distances (a few microns). The interfaces between the STO and the YSZ are seen to be atomically flat. From the high-magnification image it is possible to count the number of unit cells of STO and YSZ, nominally 25 of STO and 2 of YSZ. Most importantly, the YSZ is perfectly coherent with the STO, in agreement with x-ray diffraction (XRD) results (fig. S1), meaning that the ultrathin layer of YSZ grows rotated by 45° around the *c* axis and strains to match the STO lattice. Because the bulk lattice constants of STO and YSZ are 0.3905 (*19*) and 0.514 nm (*20*), respectively, the epitaxial growth of the YSZ on top of the STO ensures a large, expansive strain in the thin YSZ layers of 7% in the *ab* plane. Increasing the thickness of YSZ (for constant STO thickness) results in a loss of structural coherence, as reflected by a reduction of superlattice satellites in XRD. Electron microscopy observations confirm that the release of strain results in a granular morphology, although the growth remains textured.

We plotted the lateral electrical conductivity (real part σ′) of the thinnest YSZ trilayer versus frequency in a double logarithmic plot (Fig. 2). The characteristic electrical response of ionic conductors (*21*–*23*) is observed in the figure. The long range or σ_{dc} ionic conductivity of the material is obtained from the plateau found in σ′ versus frequency plots. In the presence of blocking effects due to grain boundaries or electrodes, a further

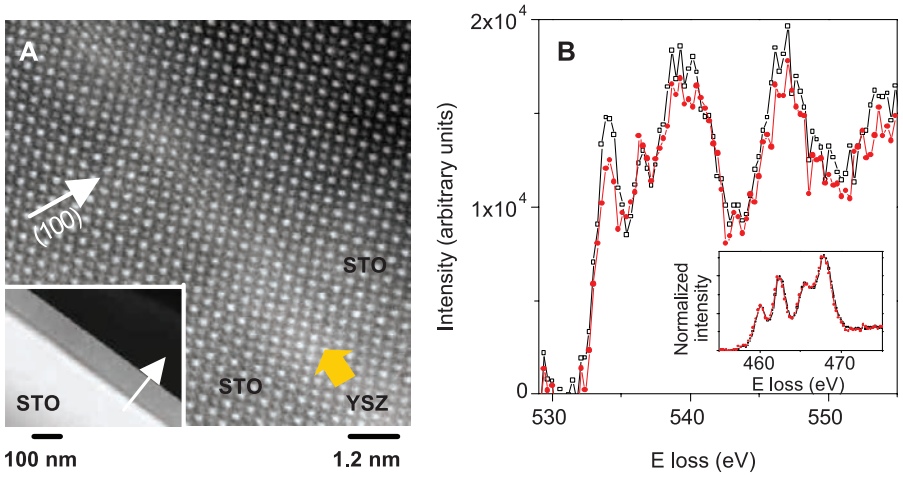

Fig. 1. (**A**) Z-contrast scanning transmission electron microscopy (STEM) image of the STO/YSZ interface of the $[YSZ_{1nm}/STO_{10nm}]_9$ superlattice (with nine repeats), obtained in the VG Microscopes HB603U microscope. A yellow arrow marks the position of the YSZ layer. (Inset) Low-magnification image obtained in the VG Microscopes HB501UX column. In both cases a white arrow indicates the growth direction. (**B**) EEL spectra showing the O K edge obtained from the STO unit cell at the interface plane (red circles) and 4.5 nm into the STO layer (black squares). (Inset) Ti $L_{2,3}$ edges for the same positions, same color code. All spectra are the result of averaging four individual spectra at these positions, with an acquisition time of 3 s each.

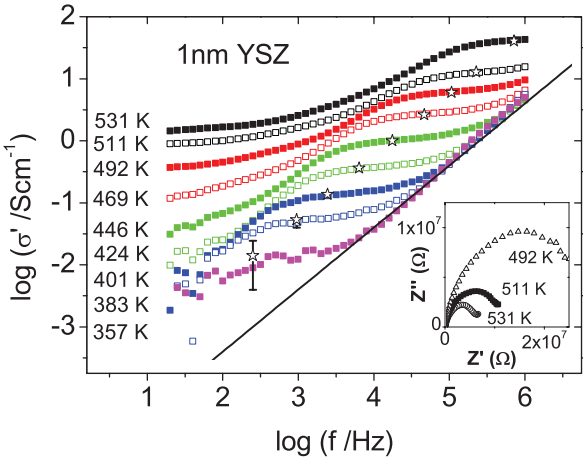

Fig. 2. Real part of the lateral electrical conductivity versus frequency of the trilayer with 1-nm-thick YSZ in a double log plot. Isotherms were measured in the range of 357 to 531 K. The solid line represents a NCL contribution ($\sigma' \sim A\omega$, where *A* is a temperature-dependent proportionality factor and ω is the angular frequency), as explained in the text. Stars identify the value of σ_{dc}. The uncertainty of conductance measurements is 1 nS (10^{-2} S/cm in conductivity for the sample shown, see error bar). (**Inset**) Imaginary versus real part of the impedance (Nyquist) plots at 492, 511, and 531 K. Whereas the high-frequency contribution is a Debye-like process characterized by a conductivity exponent $n = 0$, the "grain boundary" term observed in the Nyquist plots shows a clear deviation from a Debye behavior, as reflected by the distorted impedance arcs.

[1]Grupo de Física de Materiales Complejos, Universidad Complutense de Madrid, Madrid 28040, Spain. [2]Materials Science and Technology Division, Oak Ridge National Laboratory, Oak Ridge, TN 37831, USA. [3]Escuela Técnica Superior de Ingenieros de Telecomunicaciones, Universidad Politécnica de Madrid, Madrid 28040, Spain.

*To whom correspondence should be addressed. E-mail: jacsan@fis.ucm.es

decrease of σ′ (below bulk σ_{dc} values) may occur toward lower frequencies. For clarity, the value of σ_{dc} has been identified by using stars. The σ_{dc} value is found to be thermally activated, so when the temperature is reduced the conductivity curves shift downwards in Fig. 2. The inset in Fig. 2 displays Nyquist plots for the same sample. To determine the nature of the charge carriers, we measured the conductance of the samples by means of dc measurements. As can be observed in fig. S2, the dc conductance (open circles) is three to four orders of magnitude lower than the values obtained from ac measurements (solid squares) in the entire temperature measurement range. This result indicates that the electronic contribution to the ac measurements can be considered negligible, and thus, the measured ac transport is attributable to an ionic diffusion process.

In Fig. 3, the temperature dependence of the σ_{dc} of $[STO_{10nm}/YSZ_{Xnm}/STO_{10nm}]$ trilayers is shown together with data corresponding to a single crystal and the 700-nm thin film from (*7*). Whereas the "bulklike" samples (the thin film and the single crystal) show the well-known Arrhenius behavior with an activation energy of ~1.1 eV, the trilayers show much larger conductivity values and smaller values of the activation energy. The thickest trilayer (62-nm YSZ) already shows an increase of about two orders of magnitude in the high-temperature dc conductivity, and the dc activation energy decreases to 0.72 eV. When decreasing the thickness of the YSZ layer to 30 nm, the dc conductivity increases another three orders of magnitude, and the activation energy decreases to 0.6 eV. The high values of the pre-exponential factor of $\sim 10^{7}$ $(ohm \cdot cm)^{-1}$ are comparable to those found in other ion conductors (*24*) [see supporting online material (SOM) text]. If the thickness is further reduced all the way down to 1 nm (two unit cells of YSZ), the conductivity is observed to increase as the inverse of the YSZ layer thickness, but the conductance is essentially thickness-independent (bottom inset in Fig. 3). We can think of three parallel conduction paths due to the interfaces and the bulk YSZ and STO layers. The bulk conductivity of YSZ is 10^{-7} S/cm at 500 K, which would yield a conductance value of $\sim 10^{-14}$ S for 1-nm-thick layers. This value is much lower than the 10^{-6} S value measured with the ac technique. If we instead assume that the high conductance ($G = 10^{-6}$ S) is due to electronic conduction in the STO, both ac and dc techniques would provide this same value, contrary to what is observed (fig. S2). Moreover, reported conductivity values in STO thin films (*25*) are also much lower than those necessary to explain the high conductance observed. Because bulk YSZ or STO contributions can be ruled out, an interface conduction mechanism is inferred.

To further test this scenario, we grew superlattices repeating the $[YSZ_{1nm}/STO_{10nm}]$ growth unit. We found (top inset in Fig. 3) that conductance scales now with the number of interfaces up to a number of eight (four bilayer repetitions). There is a scaling breakdown in the figure, observed for a larger number of bilayer repetitions, most likely resulting from disorder building up in this highly strained structure. The experimental data indicates that the first STO/YSZ interface does not contribute to the large ionic conductivity observed in the samples, probably because the first STO layer is somehow different from the others as it is grown directly on the substrate. This scaling, together with the invariance of the conductance with the thickness of the YSZ, shows that the large conductivity values in these heterostructures originate truly at the interfaces between YSZ and STO. Our results indicate a superposition of two parallel contributions—one due to the bulk and one attributable to the interface—and the colossal ionic conductivity is observed as long as the interface conductance is larger than that of the bulk. The abrupt conductivity decrease when the thickness changes from 30 to 62 nm is most likely due to a degraded interface structure when the YSZ layers exceed the critical thickness.

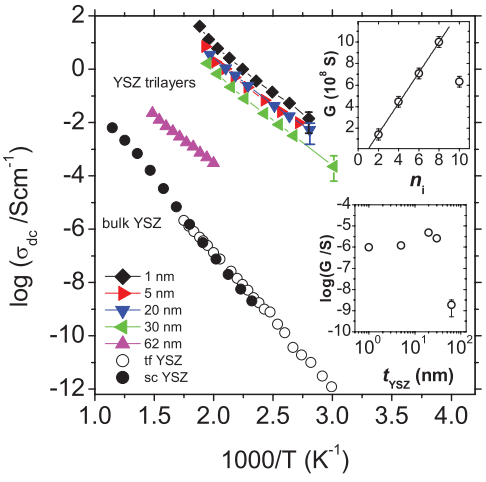

Fig. 3. Dependence of the logarithm of the long-range ionic conductivity of the trilayers STO/YSZ/STO versus inverse temperature. The thickness range of the YSZ layer is 1 to 62 nm. Also included are the data of a single crystal (sc) of YSZ and a thin film (tf) 700 nm thick [taken from (*7*)] with the same nominal composition. (**Top inset**) 400 K conductance of $[YSZ_{1nm}/STO_{10nm}]_{(ni/2)}$ superlattices as a function of the number of interfaces, n_i. (**Bottom inset**) Dependence of the conductance of $[STO_{10nm}/YSZ_{Xnm}/STO_{10nm}]$ trilayers at 500 K on YSZ layer thickness. Error bars are according to a 1 nS uncertainty of the conductance measurement.

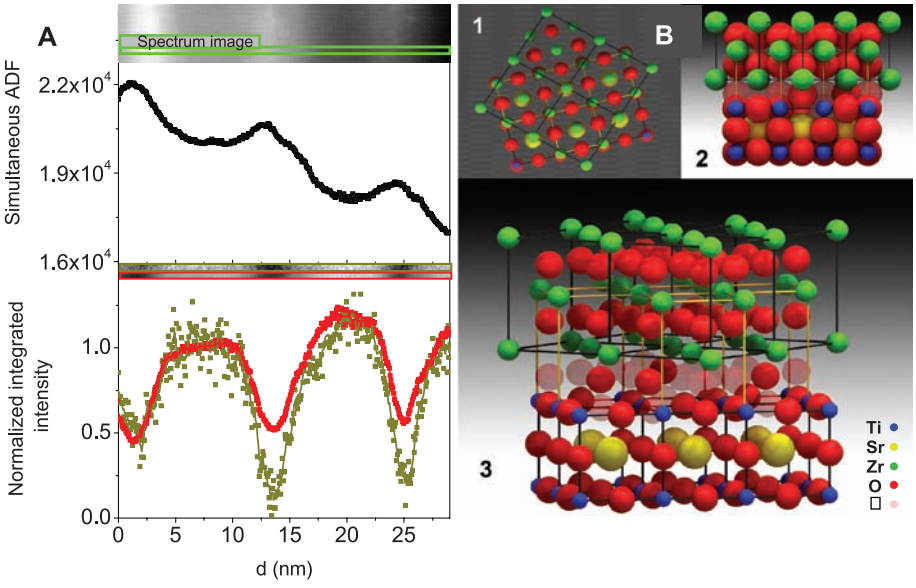

Fig. 4. (**A**) EELS chemical maps. The ADF image in the upper panel shows the area used for EELS mapping (spectrum image, marked with a green rectangle) in the $[YSZ_{1nm}/STO_{10nm}]_9$ superlattice. The middle panel shows the averaged ADF signal acquired simultaneously with the EEL spectrum image, showing the STO (low-intensity regions) and YSZ (higher-intensity) layers. The lower panel shows the Ti (red) and Sr (dark yellow) EELS line traces across several consecutive interfaces. These line traces are averaged from the elemental 2D images shown in the insets, each framed with the same color code (red for Ti, dark yellow for Sr). Data was obtained in the VG Microscopes HB501UX. Because the STEM specimen was relatively thick (several tens of nanometers), the wide chemical interface profiles are most likely attributable to beam broadening. (**B**) Solid spheres model of the YSZ/STO interface showing: (1) The compatibility of the perovskite and fluorite (rotated) structures. (2) A side view of the interface between STO (at the bottom) and YSZ (on top) with realistic ionic radius. The shaded oxygen positions in the interface plane are presumed absent or displaced because of volume constraints, enabling the high ionic conductivity. (3) A 3D view of the interface, with the ionic radius reduced by half to better visualize the plane of oxygen vacancies introduced in the interface. The square symbol in the legend indicates the empty positions available for oxygen ions at the interface.

The dc conductivity of the 1-nm YSZ layer shows a record value of 0.014 S/cm at 357 K, with an activation energy of 0.64 eV and an extrapolated value of 0.003 S/cm at 300 K. Thus, the threshold for the conductivity value that defines the feasibility for practical applications, 0.01 S/cm, is reached in these ultrathin films just slightly above room temperature. Previous enhancements of the conductivity in nanoscopic systems have been explained in terms of size effects (*13*–*16*) and overlapping of space charge regions. However, the screening or Debye length in ionic conductors with high carrier concentrations, such as YSZ, is on the order of 0.1 nm (*26*). The conductivity values found here are in good agreement with a recent prediction of Kosacki *et al*. (*17*), who analyzed thicker YSZ thin films (15 nm) grown on MgO substrates, discussing the possible existence of an interface diffusion mechanism that would yield a dc conductivity ~0.001 S/cm at room temperature, with an activation energy of 0.45 eV for a film thickness ~1.6 nm. Consequently, and considering the good epitaxial quality of the heterostructures, we believe that strain and especially interfacial effects are at the origin of the enhanced conductivity.

To further investigate the role of the interfaces in the observed increase of ~eight orders of magnitude in the ionic conductivity with respect to bulk YSZ values, we next present a detailed analysis of the YSZ/STO interfaces using atomic column resolution electron energy-loss spectroscopy (EELS). Figure 4A shows line traces corresponding to elemental concentrations of Ti and Sr obtained from EELS spectrum images of the $[YSZ_{1nm}/STO_{10nm}]_9$ superlattice across several bilayers. The YSZ layers are the bright bands observed in the annular dark field (ADF) picture in the upper inset, which also shows in a green rectangle the area used for EELS analysis. The lower panel shows the normalized integrated intensity under the Sr M_3 (dark yellow) and the Ti $L_{2,3}$ (red) absorption lines. The resulting two-dimensional (2D) images are shown in the inset. It can be observed that the Ti intensity is clearly higher than that of Sr in all of the interfaces, indicating that the STO termination layer is always a (TiO_2) plane. YSZ grows epitaxially, rotating its cell 45° to accommodate half of the diagonal of the YSZ conventional unit cell [$a_{YSZ}/\sqrt{2}$ = 0.361 nm (a_{YSZ} = 0.514 nm), where a is the lattice parameter] to the STO perovskite unit cell (a_{STO} = 0.390 nm) with a 7% in plane tensile strain on the YSZ. In this configuration, both structures are compatible because the FCC fluorite structure of YSZ keeps the positions of the atoms in the ab plane, the only difference being that the oxygen atoms of the fluorite are not in the z = 0 plane but are displaced to z = 1/4 along the c direction (Fig. 4B). The first YSZ plane in the (001) stacking sequence should be an O plane at $c_{YSZ}/4$, but these O sites are directly above the O atoms of the last TiO_2 plane. Presumably, these sites are either vacant or the O atoms are displaced from their normal positions (as suggested by the shaded sites in Fig. 4B). Therefore, this interfacial O plane is likely to be highly disordered, even though the cation lattice remains coherent, which would thereby enable the enhancement in ionic conductivity.

Further evidence for this interface structure comes from a close inspection of the fine structure of the O K edge (oxygen/potassium absorption edge) at the STO interface plane (Fig. 1B), which shows noticeable changes when compared to the O K edge from the middle of the STO layer. These changes are consistent with an enhanced density of O vacancies in this plane (*27*). However, we could not detect any change in the oxidation state of Ti at the interface (it is +4), which is in good agreement with the lack of electronic conduction observed (inset in Fig. 1B). Additionally, the fine structure of the O K edge within the YSZ ultrathin layers is completely different from that of bulk YSZ, as a consequence of the severe structural distortions in the oxygen octahedra attributable to the large strain accumulated (fig. S3 and SOM text). Thus, these results point to partial occupancy and high disorder in the interface oxygen plane, resulting in the introduction of a large number of interfacial oxygen vacancies and a substantial decrease in the activation energy for O migration. The STO side of the YSZ/STO interface may play a role in stabilizing disorder in the anionic sublattice, as has been recently reported for the $LaAlO_3/SrTiO_3$ interface (*28*, *29*).

The analysis of the high-frequency dispersive ac conductivity above the dc plateau of Fig. 2 may provide some further insight into the colossal ionic conductivity. In ionic conductors, the dc plateau crosses over into a dispersive conductivity regime depending on frequency as a power law with a fractional exponent n (n < 1). This contribution is usually known as Jonscher's response and reflects the influence of ion-ion correlations on ion motion (*21*–*23*, *30*, *31*). At even higher frequencies and lower temperatures, the power law dependence of the conductivity universally merges into an almost linear frequency-dependent term with n = 1, resulting in a regime with a nearly constant (dielectric) loss (NCL) (*32*, *33*). NCL is weakly temperature dependent and has been ascribed to caged dynamics of mobile ions at short times (high frequencies) (*34*). Both power law regimes are usually distinct, and they are observed in particular in bulk or "thick" thin films of YSZ, where the n exponent has a value of ~0.5 to 0.6 before merging into the NCL behavior (*6*, *7*). In the case of our ultrathin YSZ heterostructures, either the Jonscher's response is absent (n = 0) or n is a very small value (Fig. 2), as shown by the dc plateau directly merging into a NCL (n = 1) term, which is plotted in the figure as a solid line to guide the eye. This is a very anomalous result indicating an uncorrelated ion diffusion process. The absence of the fractional power law regime has only been observed in systems with a carrier concentration low enough so that the carriers do not interact with each other. Such an explanation can be ruled out in our samples where the large conductivity values do not, by any means, indicate a reduced carrier density. We believe that the uncorrelated ion diffusion at the interface is another manifestation of conduction along the oxygen depleted/disordered interface plane. In fact, the absence of ion-ion correlations may produce a decrease in the activation energy of the conductivity (*30*, *31*). The large in-plane expansive strain on the YSZ interface plane, together with the high concentration of vacant oxygen positions and probable positional disorder, surely contributes to the reduction in the activation energy and the resulting huge enhancement in ionic conductivity.

We have shown eight orders of magnitude enhancement of the ionic conductivity of YSZ in ultrathin films reaching values that enable practical application of the material in SOFCs slightly above room temperature. This result may have a special impact on single-chamber fuel cells where both electrodes are located on the same side of a thin electrolyte film deposited onto a substrate, and thus the ionic current flows in a lateral direction parallel to the substrate (*35*). The coherent interface between very dissimilar structures (in this case, fluorite and perovskite in YSZ/STO heterostructures) provides both a high carrier concentration and, simultaneously, a decreased activation energy, achieving a greatly enhanced mobility that accounts for the many orders of magnitude increase of the conductivity. The combination of epitaxial strain and suitable heterogeneous interfaces appears to be a key step in the design of artificial nanostructures with high ionic conductivity. This result is of major technological importance to achieve fast oxygen conduction at room temperature, and the outstanding electrical properties of the ultrathin YSZ/STO heterostructures may open the way to new and improved devices far beyond fuel cells.

References and Notes

1. B. C. H. Steele, A. Heinzel, *Nature* **414**, 345 (2001).
2. R. M. Ormerod, *Chem. Soc. Rev.* **32**, 17 (2003).
3. J. B. Goodenough, *Annu. Rev. Mater. Res.* **33**, 91 (2003).
4. J. W. Fergus, *J. Power Sources* **162**, 30 (2006).
5. W. Nernst, *Z. Elektrochem.* **6**, 41 (1899).
6. A. Pimenov, J. Ullrich, P. Lunkenheimer, A. Loidl, C. H. Ruscher, *Solid State Ionics* **109**, 111 (1998).
7. A. Rivera, J. Santamaria, C. Leon, *Appl. Phys. Lett.* **78**, 610 (2001).
8. N. P. Brandon, S. Skinner, B. C. H. Steele, *Annu. Rev. Mater. Res.* **33**, 183 (2003).
9. Z. Shao, S. M. Haile, *Nature* **431**, 170 (2004).
10. Y. Yoo, *J. Power Sources* **160**, 202 (2006).
11. H. Huang *et al*., *J. Electrochem. Soc.* **154**, B20 (2007).
12. I. Kosacki, B. Gorman, H. U. Anderson, *Electrochem. Soc. Proc.* **97**, 631 (1998).
13. T. Suzuki, I. Kosacki, H. U. Anderson, P. Colomban, *J. Am. Ceram. Soc.* **85**, 1492 (2002).
14. S. Azad *et al*., *Appl. Phys. Lett.* **86**, 131906 (2005).
15. J. Maier, *Solid State Ionics* **131**, 13 (2000).
16. N. Sata, K. Eberman, K. Eberl, J. Maier, *Nature* **408**, 946 (2000).
17. I. Kosacki, C. M. Rouleau, P. F. Becher, J. Bentley, D. H. Lowndes, *Solid State Ionics* **176**, 1319 (2005).
18. Materials and methods are available as supporting material on *Science* Online.
19. H. Swanson, R. K. Fuyat, *Natl. Bur. Stand. Circ. (US)* **3**, 44 (1954).
20. P. Li, I.-W. Chen, J. E. Penner-Hahn, *Phys. Rev. B* **48**, 10063 (1993).
21. A. K. Jonscher, *Nature* **267**, 673 (1977).
22. C. A. Angell, *Chem. Rev.* **90**, 523 (1990).
23. F. Kremer, A. Schönhals, Eds., *Broadband Dielectric Spectroscopy* (Springer, Berlin, 2003).

24. R. J. Cava, E. A. Rietman, *Phys. Rev. B* **30**, 6896 (1984).
25. C. Ohly, S. Hoffmann-Eifert, X. Guo, *J. Am. Ceram. Soc.* **89**, 2845 (2006).
26. A. Peters, C. Korte, D. Hesse, N. Zakharov, J. Janek, *Solid State Ionics* **178**, 67 (2007).
27. D. J. Wallis, N. D. Browning, *J. Am. Ceram. Soc.* **80**, 781 (1997).
28. W. Siemons *et al.*, *Phys. Rev. Lett.* **98**, 196802 (2007).
29. A. Kalabukhov *et al.*, *Phys. Rev. B* **75**, 121404(R) (2007).
30. K. L. Ngai, A. K. Rizos, *Phys. Rev. Lett.* **76**, 1296 (1996).
31. K. L. Ngai, G. N. Greaves, C. T. Moyhihan, *Phys. Rev. Lett.* **80**, 1018 (1998).
32. W. K. Lee, J. F. Liu, A. S. Nowick, *Phys. Rev. Lett.* **67**, 1559 (1991).
33. K. L. Ngai, *J. Chem. Phys.* **110**, 10576 (1999).
34. J. Habasaki, K. L. Ngai, Y. Hiwatari, *J. Chem. Phys.* **120**, 8195 (2004).
35. J. Fleig, H. L. Tuller, J. Maier, *Solid State Ionics* **174**, 261 (2004).
36. This work was supported by grants from the Spanish Ministry for Science and Innovation (MAT2005 06024, MAT2007 62162, and MAT 2008) and by the Madrid Regional Government Communidad Autónoma de Madrid through Universidad Complutense de Madrid Groups Programme. We thank U. Complutense–Centro de Asistencia a la Investigación de Técnicas Físicas for technical support. Research at Oak Ridge National Laboratory (M.V. and S.J.P.) was sponsored by the Division of Materials Sciences and Engineering of the U.S. Department of Energy. We are grateful to J. T. Luck for help with STEM specimen preparation and to F. de Andrés for help with the graphic design of the hard spheres model.

Supporting Online Material

www.sciencemag.org/cgi/content/full/321/5889/676/DC1
Materials and Methods
SOM Text
Figs. S1 to S3
References

12 February 2008; accepted 13 June 2008
10.1126/science.1156393

High-Resolution Greenland Ice Core Data Show Abrupt Climate Change Happens in Few Years

Jørgen Peder Steffensen,[1]* Katrine K. Andersen,[1] Matthias Bigler,[1,2] Henrik B. Clausen,[1] Dorthe Dahl-Jensen,[1] Hubertus Fischer,[2,3] Kumiko Goto-Azuma,[4] Margareta Hansson,[5] Sigfús J. Johnsen,[1] Jean Jouzel,[6] Valérie Masson-Delmotte,[6] Trevor Popp,[7] Sune O. Rasmussen,[1] Regine Röthlisberger,[2,8] Urs Ruth,[3] Bernhard Stauffer,[2] Marie-Louise Siggaard-Andersen,[1] Árný E. Sveinbjörnsdóttir,[9] Anders Svensson,[1] James W. C. White[7]

The last two abrupt warmings at the onset of our present warm interglacial period, interrupted by the Younger Dryas cooling event, were investigated at high temporal resolution from the North Greenland Ice Core Project ice core. The deuterium excess, a proxy of Greenland precipitation moisture source, switched mode within 1 to 3 years over these transitions and initiated a more gradual change (over 50 years) of the Greenland air temperature, as recorded by stable water isotopes. The onsets of both abrupt Greenland warmings were slightly preceded by decreasing Greenland dust deposition, reflecting the wetting of Asian deserts. A northern shift of the Intertropical Convergence Zone could be the trigger of these abrupt shifts of Northern Hemisphere atmospheric circulation, resulting in changes of 2 to 4 kelvin in Greenland moisture source temperature from one year to the next.

Ice core records from Greenland have been instrumental in investigating past abrupt climate change. As compared with other sedimentary records, the ice core records have unparalleled temporal resolution and continuity (*1*–*3*). The newest Greenland ice core, from the North Greenland Ice Core Project (NGRIP), has been measured at very high resolution for water isotope ratios, dust, and impurity concentrations. This allows researchers for the first time to follow the ice core proxies of Greenland temperature, accumulation, moisture origin, and aerosol deposition at subannual resolution over the very abrupt climate changes in the period from 15.5 to 11.0 thousand years ago (ka) (measured from 2000 AD throughout this study).

In the Northern Hemisphere, the last glacial period ended in a climatic oscillation composed of two abrupt warmings interrupted by one cooling event (*3*–*6*). The temperature changed rapidly from glacial to mild conditions in the Bølling and Allerød periods and then returned to glacial values in the Younger Dryas period before the onset of the present warm interglacial, the Holocene (Fig. 1, and see table S1 for classification of climate periods). The shape and duration of the abrupt climate change at the termination of the last glacial have previously been constrained by Greenland ice core records from DYE-3 (*4*, *7*), Greenland Ice Core Project (GRIP) (*8*) and Greenland Ice Sheet Project 2 (GISP2) (*3*, *6*, *9*), but sampling of these cores did not typically achieve a resolution sufficient to resolve annual layers. Because of new continuous flow analysis (CFA) systems (*10*–*12*), impurity and chemical records of the recent NGRIP ice core (*1*) have been obtained at subannual resolution, which allows for the multiple-proxy identification of annual-layer thickness and the construction of a new Greenland time scale, the Greenland Ice Core Chronology 2005 (GICC05) (*2*). Complementary highly detailed stable water isotope profiles ($\delta^{18}O$ and δD) have been measured on the NGRIP ice core covering the period from 15.5 to 11.0 ka at 2.5-to-5.0-cm resolution, corresponding to one to three samples per year. They were compared with the concentrations of insoluble dust, soluble sodium (Na^+), and calcium (Ca^{2+}), each measured with CFA at subannual resolution (*10*, *12*, *13*) (Fig. 2) and, when available, with the highest-resolution data from GRIP, GISP2, and DYE-3 ice cores on the GICC05 time scale.

Across the warming transitions, the records exhibit clear shifts between two climate states. We characterize a shift to be significant if the mean values of the climate states on each side of the shift differ by more than the statistical standard error of the noise of a 150-year period of these climate states. A simple but objective approach to finding the best timing of the transition is to characterize the shift observed in each proxy as a "ramp": a linear change from one stable state to another. We applied a ramp-fitting method (*14*) to determine the timing of the transitions. The method entails using weighted least-squares regression to determine the ramp location and a bootstrap simulation to estimate the uncertainty of the results [transition times are listed in Table 1; see supporting online material (SOM) methods and table S2 for more detailed information on the method and the ramp fit values and uncertainties (*15*)]. Data and fitted ramps are shown in Figs. 2 and 3. For annual layer thickness (λ), concentrations of dust, Ca^{2+}, and Na^+, logarithmic scales were used because these proxies are approximately log-normally distributed.

The $\delta^{18}O$ record is a proxy for past air temperature at the ice core site (*16*, *17*). Although the magnitude of Greenland $\delta^{18}O$ changes can be influenced by changing site and source temperatures and by snowfall seasonality (*16*, *18*, *19*), the timing of $\delta^{18}O$ changes is dominated by the changing site temperature (*18*). The $\delta^{18}O$ warming transition at 14.7 ka was the most rapid and occurred within a remarkable 3 years, whereas the

[1]Centre for Ice and Climate, Niels Bohr Institute, University of Copenhagen, Juliane Maries Vej 30, DK-2100 Copenhagen OE, Denmark. [2]Climate and Environmental Physics, Physics Institute, University of Bern, Sidlerstrasse 5, CH-3012, Switzerland. [3]Alfred-Wegener-Institute for Polar- and Marine Research (AWI), Postfach 120161, D-27515 Bremerhaven, Germany. [4]National Institute of Polar Research, Kaga 1-9-10, Itabashi-ku, Tokyo 173-8515, Japan. [5]Department of Physical Geography and Quaternary Geology, Stockholm University, S-106 91, Stockholm, Sweden. [6]Institut Pierre Simon Laplace/Laboratoire des Sciences du Climat et de l'Environnement, Commissariat à l'Énergie Atomique (CEA)–CNRS–Université de Versailles Saint Quentin en Yvelines, CEA Saclay, 91191 Gif-Sur-Yvette, France. [7]The Institute of Arctic and Alpine Research, Campus Box 450, University of Colorado, Boulder, CO 80309-0450, USA. [8]British Antarctic Survey, Natural Environment Research Council, High Cross, Madingley Road, Cambridge CB3 0ET, UK. [9]Raunvísindastofnun Háskólans, Dunhagi 3, Iceland.

*To whom correspondence should be addressed. E-mail: jps@gfy.ku.dk